

# JAAS

Accepted Manuscript



This is an *Accepted Manuscript*, which has been through the Royal Society of Chemistry peer review process and has been accepted for publication.

*Accepted Manuscripts* are published online shortly after acceptance, before technical editing, formatting and proof reading. Using this free service, authors can make their results available to the community, in citable form, before we publish the edited article. We will replace this *Accepted Manuscript* with the edited and formatted *Advance Article* as soon as it is available.

You can find more information about *Accepted Manuscripts* in the [Information for Authors](#).

Please note that technical editing may introduce minor changes to the text and/or graphics, which may alter content. The journal's standard [Terms & Conditions](#) and the [Ethical guidelines](#) still apply. In no event shall the Royal Society of Chemistry be held responsible for any errors or omissions in this *Accepted Manuscript* or any consequences arising from the use of any information it contains.

## Simultaneous 3-Dimensional Elemental Imaging with LIBS and LA-ICP-MS

Jose R. Chirinos<sup>1</sup>, Dayana D. Oropeza<sup>1</sup>, Jhanis J. Gonzalez<sup>1,2</sup>, Huaming Hou<sup>1</sup>, Mark Morey<sup>3</sup>,

Vassilia Zorba<sup>1</sup> and Richard E. Russo<sup>1,2</sup>

<sup>1</sup> Lawrence Berkeley National Laboratory, Berkeley, CA 94720, USA

<sup>2</sup> Applied Spectra, 46661 Fremont Blvd., Fremont, CA 94538, USA

<sup>3</sup> Special Technologies Laboratory, Santa Barbara, CA 93111, USA

### Abstract

Laser Induced Breakdown Spectroscopy (LIBS) and Laser Ablation Inductively Coupled Plasma–Mass Spectrometry (LA-ICP-MS) are used simultaneously for spatially resolved mapping of major and trace elements and isotopes within a *Bastnäs* rare earth ore sample. The combination of the two techniques provides complementary measurements for elements that are separately unattainable due to low sensitivity and/or strong interferences. Two dimensional (2D) layer-by-layer mapping, 2D cross-sectional imaging and three-dimensional (3D) volume rendering of elements and isotopes in the *Bastnäs* matrix are presented. These results pave the way for improved 3D elemental imaging through simultaneously acquired LIBS and LA-ICP-MS measurements.

**Keywords:** *Elemental Imaging, Isotopic Imaging, LA-ICP-MS, LIBS, Laser Ablation, 3D Mapping, Geological samples.*

## Introduction

Laser Ablation Inductively Coupled Plasma–Mass Spectrometry (LA-ICP-MS) is a powerful direct solid sampling analytical technique for high sensitivity, and precision elemental and isotopic analysis of materials. The process involves a high-power pulsed laser beam directed and focused onto a sample to instantaneously convert a finite volume of the sample into vapor and aerosol constituents (laser ablation) for analysis, followed by transport and excitation of the ablated aerosol to a secondary source (ICP), before entering a mass spectrometer (MS)<sup>1,2,3,4</sup>. Predominantly used in micro and bulk analysis, LA-ICP-MS has emerged in recent years as a chemical imaging technique where individually sampled spots are correlated to spatially assigned coordinates to produce maps of elements and isotopes. Elemental and isotopic surface (2D) mapping with LA-ICP-MS have been adopted for qualitative and quantitative elemental and isotopic imaging in biochemical applications,<sup>5</sup> ecotoxicology samples,<sup>6</sup> material science,<sup>7</sup> archeology<sup>8</sup> and geochemistry.<sup>9</sup>

Despite the tremendous advances in the sensitivity and resolution of mass analyzers coupled to the ICP source<sup>10</sup> certain elements and isotopes remain largely unmeasurable with LA-ICP-MS. Recurring limiting factors include isobaric and polyatomic interferences, abundance sensitivity and detector saturation which forces masking of specific element masses, and reduced sensitivity due to insufficient ionization of high-ionization potential elements in the argon ICP plasma. These parameters collectively make the detection of elements such as F, O, H, N, Si, Se, As, Ca, S, with conventional LA-ICP-MS systems very challenging or impossible. As a result, complementary information on these elements is usually provided independently by *ex situ* bulk or surface analysis techniques such as XRF,<sup>11</sup> EDX,<sup>12</sup> Fluorescence,<sup>13</sup> Raman,<sup>14</sup> etc. prior to LA-

1  
2  
3 ICP-MS sampling. However, cross-correlation between exact sample locations, excitation  
4 volumes and resolution (spatial and depth) -which may vary substantially and across different  
5 length-scales depending on the *ex situ* analytical technique of choice- can be challenging. Exact  
6 control of all these parameters is instrumental in the reliability and consistency of data combined  
7 from independent analytical techniques, especially for inhomogeneous samples.  
8  
9

10  
11  
12  
13  
14  
15  
16 Laser Induced Breakdown Spectroscopy or LIBS is a type of optical emission spectroscopy  
17 that provides elemental information by analyzing the spectral content of a plasma resulting from  
18 the interaction of a high-power laser pulse with a material.<sup>15,16,17</sup> The laser sampling process is  
19 identical to that used in LA-ICP-MS providing the ability to combine LIBS with LA-ICP-MS for  
20 simultaneous chemical analysis from the exact same plasma (sampled mass).  
21  
22  
23  
24  
25  
26

27  
28  
29 Combining LIBS and LA-ICP-MS is a fairly new concept reported in selected studies  
30 limited on surface chemical mapping of materials. Novotný et al. studied the elemental  
31 distribution of plant tissues and granite samples using 2D maps.<sup>18,19,20,21</sup> In these reports the two  
32 techniques were used independently by ablating nearby sample locations and with different laser  
33 and detection systems therefore no elemental correlation was possible. In contrast, Lackoczy and  
34 Ghislain presented 2D maps of magnesium based alloys.<sup>22</sup> The data were obtained  
35 simultaneously and due to signal correlation they were able to use Fe mass spectrometry signals  
36 to normalize the emission, and reported an improvement on limit of detection of one order of  
37 magnitude In this work, we use simultaneous LIBS/LA-ICP-MS to chemically correlate, image  
38 and map major and trace elements and isotopes through 2D layer-by-layer and 2D cross-  
39 sectional imaging as well as 3D volume reconstruction of the elemental distribution in geological  
40 samples. This approach adds the capability of 3D elemental and isotopic mapping of a solid  
41  
42  
43  
44  
45  
46  
47  
48  
49  
50  
51  
52  
53  
54  
55  
56  
57  
58  
59  
60

1  
2  
3 sample by implementing advanced visualization and correlation techniques. A rare earth element  
4 (REE)-rich mineral sample of *Bastnäsite*<sup>23</sup>, (Ce,La)(CO<sub>3</sub>)F, was sectioned with a diamond saw  
5 and mapped simultaneously using LIBS and LA-ICP-MS. Complementary data acquired from  
6 each technique were merged and overlaid for broad chemical information imaging. The  
7 combination of LIBS and LA-ICP-MS opens new capabilities for 2D and 3D visualization of  
8 elements and isotopes in material matrices with expanded dynamic range.  
9  
10  
11  
12  
13  
14  
15  
16  
17  
18  
19  
20

## 21 **1. Experimental Methods**

22  
23  
24 A *Bastnäsite* mineral sample was obtained from the MolyCorp Mountain Pass deposit in  
25 southeastern California, USA. *Bastnäsite* REE ore was chosen due to its heterogeneity and wide  
26 elementary content including most of the lanthanides and some actinides. This sample contains a  
27 suite of elements and isotopes with a wide range of bulk concentration, from low parts per  
28 million to high percentage levels<sup>23</sup>. A sample with such a variety of elements present provides a  
29 good test for applicability range and matrix interference effects. The sample was sectioned with a  
30 diamond saw and cleaned with an ultrasonic water bath. The experimental system consisted of a  
31 laser ablation system (J100 Applied Spectra, Inc.) coupled to a Time-Of-Flight Mass  
32 Spectrometer from GBC Scientific (**Figure 1**). The laser ablation system consisted of a  
33 frequency quintupled Nd:YAG nanosecond (ns) laser at 213 nm which was focused on the  
34 sample surface by a UV microscope objective lens. Spatially resolved 3-D chemical imaging  
35 with LIBS and LA-ICP-MS was achieved by scanning the sample across 3-axis (x,y,z) with  
36 respect to the laser beam using high-precision motorized stages (resolution of 100 nm). The  
37 crater diameter was 35 μm with an average depth resolution of 3 μm /pulse. The distance  
38  
39  
40  
41  
42  
43  
44  
45  
46  
47  
48  
49  
50  
51  
52  
53  
54  
55  
56  
57  
58  
59  
60

1  
2  
3 between consecutive sampled spots was 50  $\mu\text{m}$  to ensure lack of overlap between sampling  
4 locations while maintaining a close distance between neighboring locations. The system was  
5 carefully optimized to obtain the highest sensitivity based on a NIST 612 glass sample. Five  
6 individual layers were analyzed to create layer-by-layer elemental maps with simultaneous LIBS  
7 and LA-ICP-MS. The LIBS system had a collection angle of  $45^\circ$ . Prior to the experiments we  
8 verified that side collection did not limit or influence the LIBS signal collection plane and  
9 spectral emission imaging for the sampling depth used in this study. Each of the five layers  
10 produces a 10 x 10 matrix of data corresponding to an  $0.785 \times 0.785 \text{ mm}^2$  area. Following  
11 analysis, white-light interferometry (Zygo NewView 6K) was used to determine the laser  
12 sampling characteristics.  
13  
14  
15  
16  
17  
18  
19  
20  
21  
22  
23  
24  
25  
26

27 Laser ablated particles were transported from the ablation chamber to the ICP-Time of  
28 Flight-Mass Spectrometer (ICP-TOF-MS) (GBC Scientific Optimass 9000) using helium as a  
29 carrier gas, while argon was added to the gas stream as a make-up gas. The ablation delay time  
30 between consecutive sampling locations was 10 seconds to avoid the mix of particles in the ICP-  
31 MS originating from different ablation events. The plasma optical emission (LIBS) from the  
32 laser-sampling location was imaged onto an optical fiber bundle by using a UV fused silica  
33 plano-convex lens, with the fiber directly connected to the slit entrance of a spectrometer/ICCD  
34 camera system (Acton 2150/Princeton Instruments). The gate of the ICCD camera was triggered  
35 by the ns-laser and the relative delay was controlled by the ICCD. The experimental conditions  
36 are listed in detail in **Table 1**.  
37  
38  
39  
40  
41  
42  
43  
44  
45  
46  
47  
48  
49

50 Prior to LIBS/LA-ICP-MS sampling, the morphology of the *Bastnäs*ite sample was  
51 measured using dark-field optical microscopy (Olympus BX51). The laser ablation process was  
52 monitored using a variable optical zoom system coupled to a CCD camera. Following data  
53  
54  
55  
56  
57  
58  
59  
60

1  
2  
3 acquisition the LIBS and LA-ICP-MS signals were integrated and reassigned to xyz spatial  
4  
5 coordinates to produce layer-by-layer 2D elemental maps.  
6  
7

8  
9 For 3D imaging, a series of visualization techniques were used including color-coding,  
10  
11 voxel definition and density dependent opacity. Voxel, short for volume pixel refers to the  
12  
13 smallest distinguishable box-shaped part of a three-dimensional image. Stacks of 2D surface  
14  
15 elemental maps were produced for every element of interest and served as volumetric datasets.  
16  
17 These datasets are used to add depth to an image (voxelization). In 3D imaging, voxels must  
18  
19 further undergo opacity transformation, a procedure that provides voxels different transparency  
20  
21 based on their individual values. This transformation exposes interior details of an image that  
22  
23 would otherwise be concealed by darker and more opaque outer-layer voxels. These  
24  
25 visualization methods were adopted to create overlays of multiple elements in 2D surface, 2D  
26  
27 cross-sectional and 3D volume elemental images using imaging data examiner software (Amide).  
28  
29  
30  
31  
32  
33  
34

## 35 **2. Results and Discussion**

### 36 *2.1 Simultaneous 2-D surface mapping with LIBS and LA-ICP-MS*

37  
38 LIBS optical emission acquisition was focused on the spectral window from 284 to 333 nm  
39  
40 where some of the strongest Si, Ca and Al lines could be measured (**Figure 2a**). Multiple atomic  
41  
42 and/or ionic lines of elements found in the same spectral window (Ca II 315.88 and 317.93 nm,  
43  
44 Al I 308.21 and 309.27/309.28 nm) were used to cross-verify the distribution of elements. The  
45  
46 ICP-TOF-MS allowed detection and analysis of most elements up to mass 240 as shown in  
47  
48 **Figure 2b**. The LIBS and LA-ICP-TOF-MS spectra shown in **Figure 2a** and **b** were acquired  
49  
50 simultaneously from the same location of the *Bastnäs* section.  
51  
52  
53  
54  
55  
56  
57  
58  
59  
60

1  
2  
3  
4  
5  
6  
7  
8  
9  
10  
11  
12  
13  
14  
15  
16  
17  
18  
19  
20  
21  
22  
23  
24  
25  
26  
27  
28  
29  
30  
31  
32  
33  
34  
35  
36  
37  
38  
39  
40  
41  
42  
43  
44  
45  
46  
47  
48  
49  
50  
51  
52  
53  
54  
55  
56  
57  
58  
59  
60

**Figures 2 (c)-(d)** show the 2D contour surface plots of Ca signals for the first 3  $\mu\text{m}$  from the *Bastnäs*ite cut surface. The Ca II emission line at 315.89 nm was used to construct the surface plot shown in **Figure 2c**. **Figure 2d** shows the  $^{44}\text{Ca}$  signal from the ICP-TOF-MS map reconstruction. The second highest abundance at  $^{44}\text{Ca}$  (2.086%) was chosen because  $^{40}\text{Ca}$ , which has the highest natural abundance (96.94%), interferes with  $^{40}\text{Ar}$ . On the contrary, LIBS is highly sensitive to Ca. As a result, the sensitivity and signal-to-noise ratios for the  $^{44}\text{Ca}$  signal with LA-ICP-MS are inferior to those of LIBS. Overall strong correlation is demonstrated between the two signal distributions across the  $0.785 \times 0.785 \text{ mm}^2$  surface area (**Figure 2**). The differences in the Ca elemental distributions shown in **Figure 2** could be attributed to the difference in the sensitivity of between the two techniques.

**Figure 3** depicts the surface contour maps for elements measured by LIBS in the 284-333 nm spectral range (a)-(c) and LA-ICP-MS (d)-(i) respectively. Maps of Si I (288.1 nm), Ca II (315.9 nm) and Al I (308.2 nm) are shown in (a)-(d). Out of the  $\sim 115$  masses detected and analyzed with the ICP-TOF-MS we selected to show maps of  $^{140}\text{Ce}$ ,  $^{139}\text{La}$ ,  $^{146}\text{Nd}$ ,  $^{208}\text{Pb}$  and  $^{55}\text{Mn}$  for brevity. These elements were selected for their wide range of concentration in this sample, from low parts per millions to high percentage levels.<sup>23</sup>

Specific distribution correlations are observed for the selected elements. Correlated groups include Ce, La, Nd and Al, and Mn and Fe. For these elements, high-intensities are measured in the same locations of the rock sample. Elements such as Pb and Ca appear in high concentrations in other locations of the sample and with a varying distribution as compared with the aforementioned groups. The combinations of these element groups are associated with different rock phases.<sup>23</sup>

## 2.2 Layer-by layer contour plots, cross-sectional imaging and 3-D elemental imaging with LIBS and LA-ICP-MS

Layer-by-layer chemical imaging provides important information on the elemental distribution of materials as a function of depth. This aspect of chemical imaging is increasingly important the more inhomogeneous is the sample. LIBS and LA-ICP-MS both feature layer-by-layer mapping (a combination of surface mapping and depth profiling) that allows imaging the distribution of elements in volume. Layer-by layer contours produced from the same sample at different depths from the surface using LIBS and LA-ICP-MS are shown in **Figure 4**. For brevity, only 4 elements are shown – Si I (288.1 nm) and Ca II (315.9 nm) for LIBS and  $^{238}\text{U}$  and  $^{140}\text{Ce}$  for LA-ICP-MS. These layers represent the first 15  $\mu\text{m}$  from the sample surface. Small variations were found in the Si distribution as a function of depth. However more pronounced differences were observed in the elemental distribution for Ca, U and Ce as a function of depth.

As the number of layers and data points per element increases, extended visualization capabilities are required to address the dimensionality of the problem. Basic principles of computed tomography were adopted to visualize the distribution of the selected elements in the *Bastnäs* ore matrix. Reconstruction of 3D distribution of Si, Ca and U involved color-coding, voxel conversion and allocation, as well as integrated intensity (ICP-MS counts or LIBS emission) opacity on each point. **Figure 5a** shows a merged overlay of the three elements of interest; U measured by LA-ICP-MS and Ca and Si measured by LIBS. This image represents the third layer analyzed corresponding to 9  $\mu\text{m}$  from the sample surface. The red lines across the image correspond to the horizontal and vertical locations along which the cross-sectional 2D

1  
2  
3 images of **Figure 5b** are acquired. The merged overlays of LIBS and LA-ICP-MS data in **Figure**  
4 **5b** show the elemental distributions at the selected vertical and horizontal cross sections. Distinct  
5  
6 differences in the distribution of each of the selected three elements are observed as a function of  
7  
8 depth. This distribution also varies as function on the exact location of the cross section (red  
9 lines in **Figure 5a**). Volume reconstruction allows visualization of elements in a material matrix  
10 enabling 3D chemical imaging and includes all analytical datasets. A merged overlay of the 3D  
11 volume reconstruction is shown in **Figure 5c**, with colors corresponding to the following  
12 elements: U-red, Ca-green, Si-blue.

### 23 24 25 26 *2.3 Discussion*

27  
28 Visualization of elements in 3D becomes more elaborate as the number of data points per  
29 element increases, a result of improved resolution requirements. Inevitably, resolution, both  
30 spatial and depth (or axial), is a key factor in the quantity of data generated and is related to the  
31 sample physical characteristics (e.g. roughness, porosity, etc.). Tightly focused laser beams  
32 enable analysis of small sample areas and minimization of the amount of material removed,<sup>24</sup>  
33 thereby improving the resolution in LIBS/LA-ICP-MS analysis and in spatially resolved  
34 chemical imaging. However, there are cases in which high lateral resolution (less than 10  $\mu\text{m}$ ) is  
35 not necessary and speed of analysis may be more important, for example in large-area scale  
36 analysis.

37  
38  
39  
40  
41  
42  
43  
44  
45  
46  
47  
48  
49  
50  
51  
52  
53  
54  
55  
56  
57  
58  
59  
60  
LIBS and LA-ICP-MS signal acquisition in this study were synchronized to occur from the  
same location (spot) and plasma. LIBS is an inherently faster technique than LA-ICP-MS; the  
main reason for this is that LIBS is based on measuring light from the laser induced plasma

1  
2  
3 within microseconds after the laser pulse and does not require the lag time to transport particles  
4 from the ablation chamber to the ICP-MS. For ICP-MS, the time for particle evacuation  
5 (washout time) from the chamber depends on the total mass ablated, particle size, chamber  
6 volume, gas flow rate and sampling pattern. These are the main factors limiting the speed of  
7 analysis in spatially resolved elemental and isotopic imaging, and typically restrict the laser  
8 repetition rate to 1-5Hz. However, other factors such as the transport tubing characteristics (e.g.  
9 length, internal diameter, etc.) could delay the particle entrainment into the plasma and influence  
10 the overall time of the analysis.  
11  
12  
13  
14  
15  
16  
17  
18  
19  
20  
21  
22

23 In this study, the spectral range in LIBS acquisition was 50 nm (284-333 nm). However, the  
24 use of broadband optical spectrometers i.e. Echelle or multichannel Czerny-Turner systems that  
25 cover extended spectral ranges (200-900 nm) can enable identification of even more elements of  
26 interest in a sample. The use of broadband spectrometers in LIBS will provide a wider dynamic  
27 range of complementary information to LA-ICP-MS when the two techniques are used  
28 simultaneously. Finally, new developments in the field can be used in conjunction with  
29 LIBS/LA-ICP-MS in the next generation of laser-based analytical tools. For example Laser  
30 Ablation Molecular Isotopic Spectrometry (LAMIS),<sup>25</sup> a new technology that allows direct  
31 isotopic analysis in the laser-induced plasma in real time and at atmospheric pressure, combined  
32 with LIBS/LA-ICP-MS could enable significant improvements in sensitivity and precision of  
33 laser ablation-based chemical imaging.  
34  
35  
36  
37  
38  
39  
40  
41  
42  
43  
44  
45  
46  
47  
48  
49  
50  
51  
52

### 53 **3. Conclusion**

54  
55  
56  
57  
58  
59  
60

1  
2  
3 The combination of LIBS and LA-ICP-MS has the potential of providing expanded elemental  
4 coverage from a single sampling event. We demonstrated the simultaneous use of LIBS and LA-  
5 ICP-MS as a multifunctional platform for broad chemical information analysis with 2D and 3D  
6 imaging capabilities. Computed tomography imaging principles were adopted to visualize  
7 multiple elemental and isotopic distributions in a *Bastnäs*ite mineral ore matrix.  
8  
9  
10  
11  
12  
13  
14  
15  
16  
17  
18

### 19 **Acknowledgements**

20  
21  
22 This work has been support by the Chemical Science Division, Office of Basic Energy Sciences  
23 of the U.S. Department of Energy under contract number DE-AC02-05CH11231 at the Lawrence  
24 Berkeley National Laboratory. The Special Technologies Laboratory thanks the U.S. Department  
25 of Energy's National Nuclear Security Administration, Office of Defense Nuclear  
26 Nonproliferation Research and Development, for financial support. Applied Spectra, Inc.  
27 acknowledges support from the Special Technologies Laboratory.  
28  
29  
30  
31  
32  
33  
34  
35  
36  
37  
38  
39  
40  
41  
42  
43  
44  
45  
46  
47  
48  
49  
50  
51  
52  
53  
54  
55  
56  
57  
58  
59  
60

**Table 1.** Experimental conditions.

---

**ICP-TOF-MS system (GBC Scientific)**

RF power	1200W
Plasma Ar flow rate	12.0 L min <sup>-1</sup>
Auxiliary Ar flow rate	0.60 L min <sup>-1</sup>
Acquisition parameters	
Acquisition time	200 ms
Acquisition rate	29.41 kHz
Total spectra per reading	5882

---

**Laser ablation /translation stage system**

Wavelength	213 nm
Pulse length	5 ns
Repetition rate	1 Hz
Energy per pulse	6 mJ
Spot size	35 μm
Number of laser passes	5
Number of locations/pass	225
Total sampled area	0.785 x 0.785 mm <sup>2</sup>

---

**Optical spectrometer system (Czerny Turner)**

Grating	2400 gr/mm
Center wavelength	310nm
Gate width	3.0 μs
Gate delay	800 ns
Carrier(He)/make-up (Ar) flow rate	0.90/0.90 L min <sup>-1</sup>

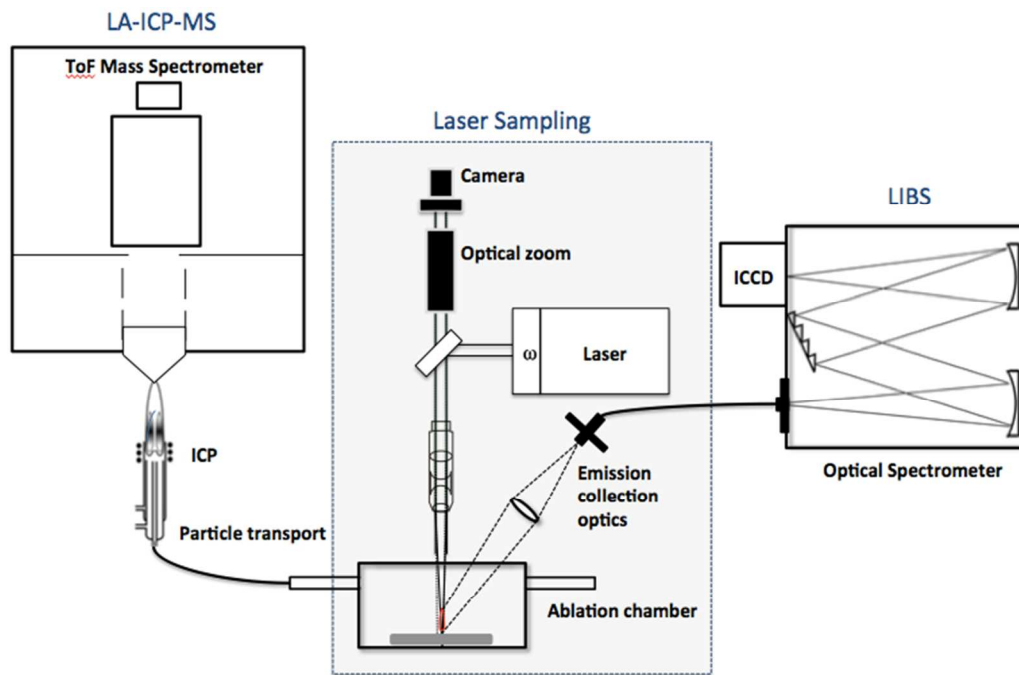


**Figure 1.** Experimental setup for simultaneous LIBS and LA-ICP-MS.

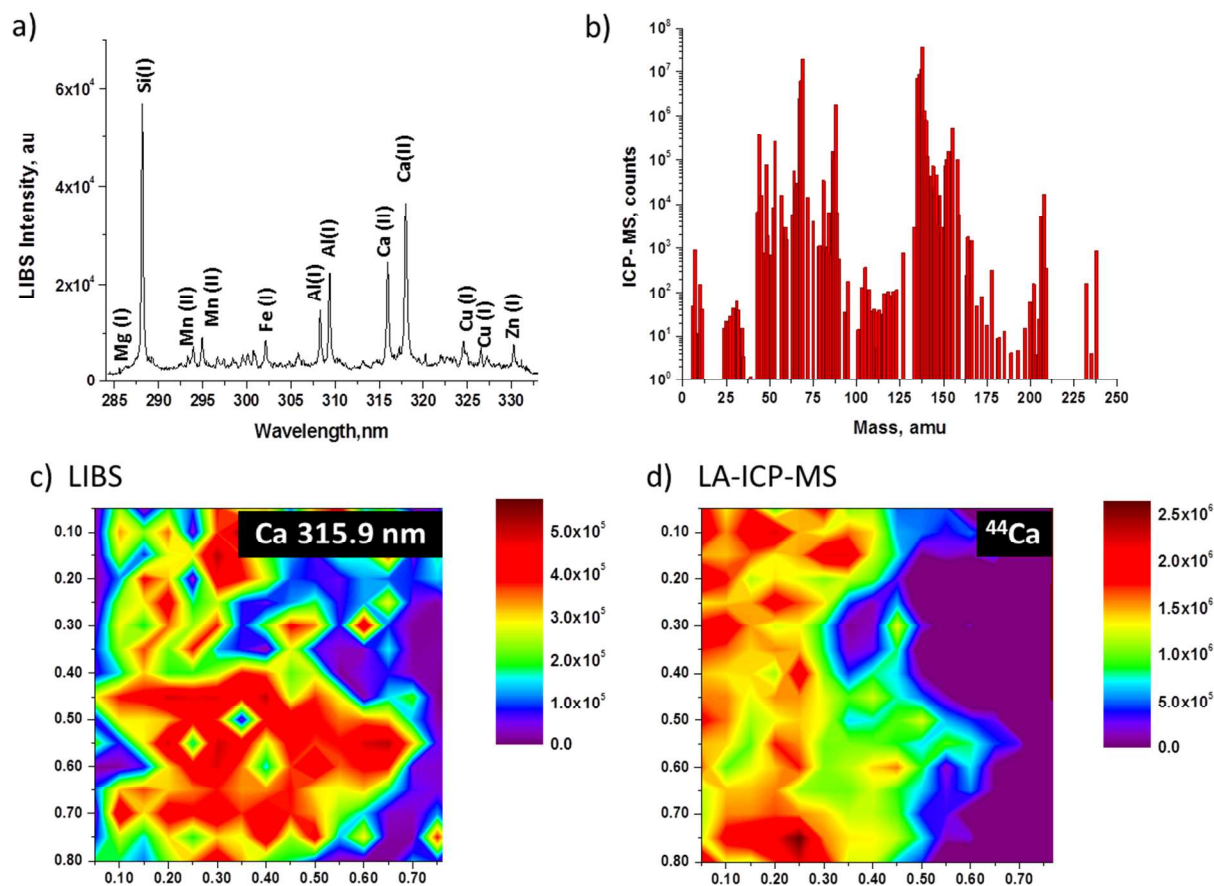


**Figure 2.** Representative LIBS (a) and LA-ICP-MS (b) spectra acquired from a single location of the sample. (c)-(d) Surface (2D) distribution of Ca of the same  $0.785 \times 0.785 \text{ mm}^2$  area of a *Bastnäsite* rock sample. The Ca maps were obtained simultaneously by (c) LIBS and (d) LA-ICP-MS.

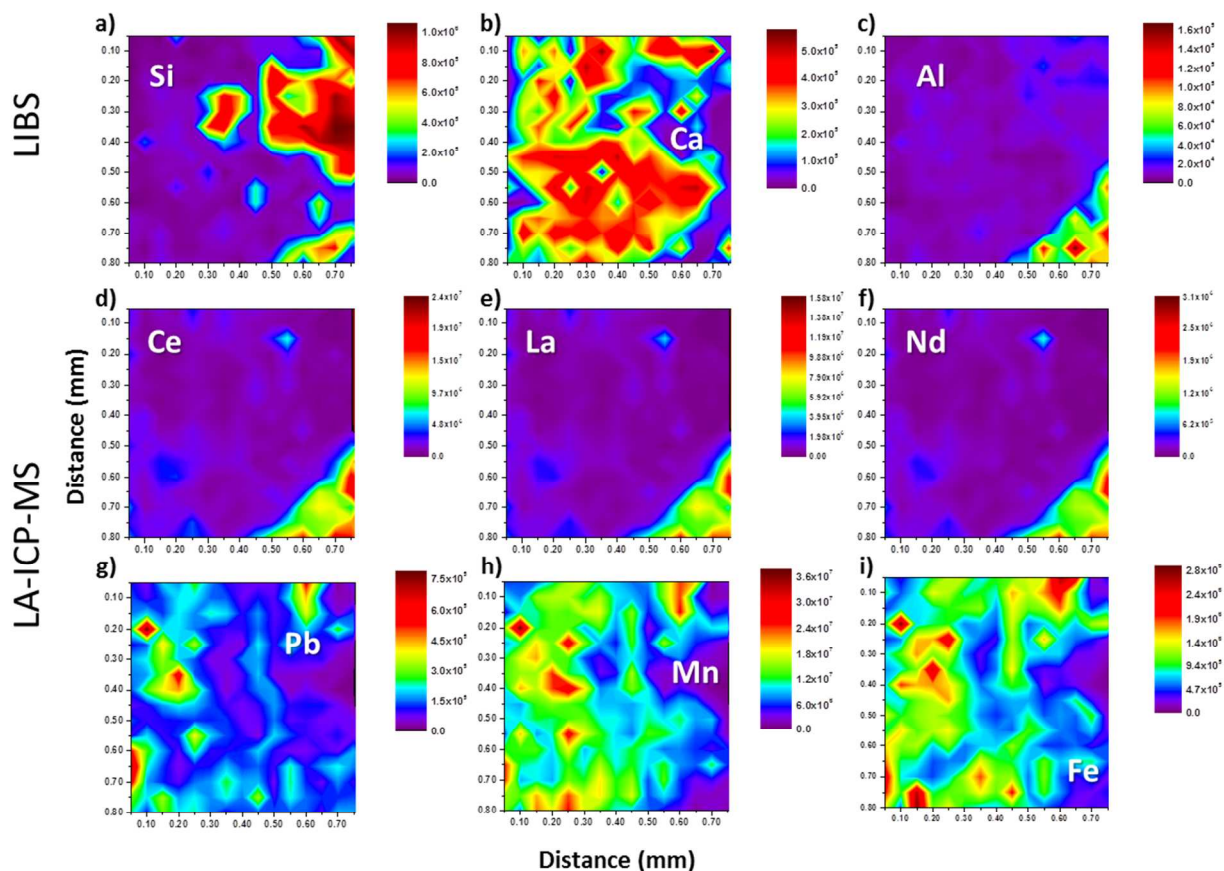


**Figure 3.** Simultaneously obtained 2D LIBS surface maps of the *Bastnäsite* rock sample using LIBS and LA-ICP-MS. (a)-(c) LIBS elemental maps of Si I (288.1 nm), Ca II (315.9 nm) and Al I (308.2 nm). (d)-(i) LA-ICP-MS maps of  $^{140}\text{Ce}$ ,  $^{139}\text{La}$ ,  $^{146}\text{Nd}$ ,  $^{208}\text{Pb}$ ,  $^{55}\text{Mn}$  and  $^{57}\text{Fe}$ .

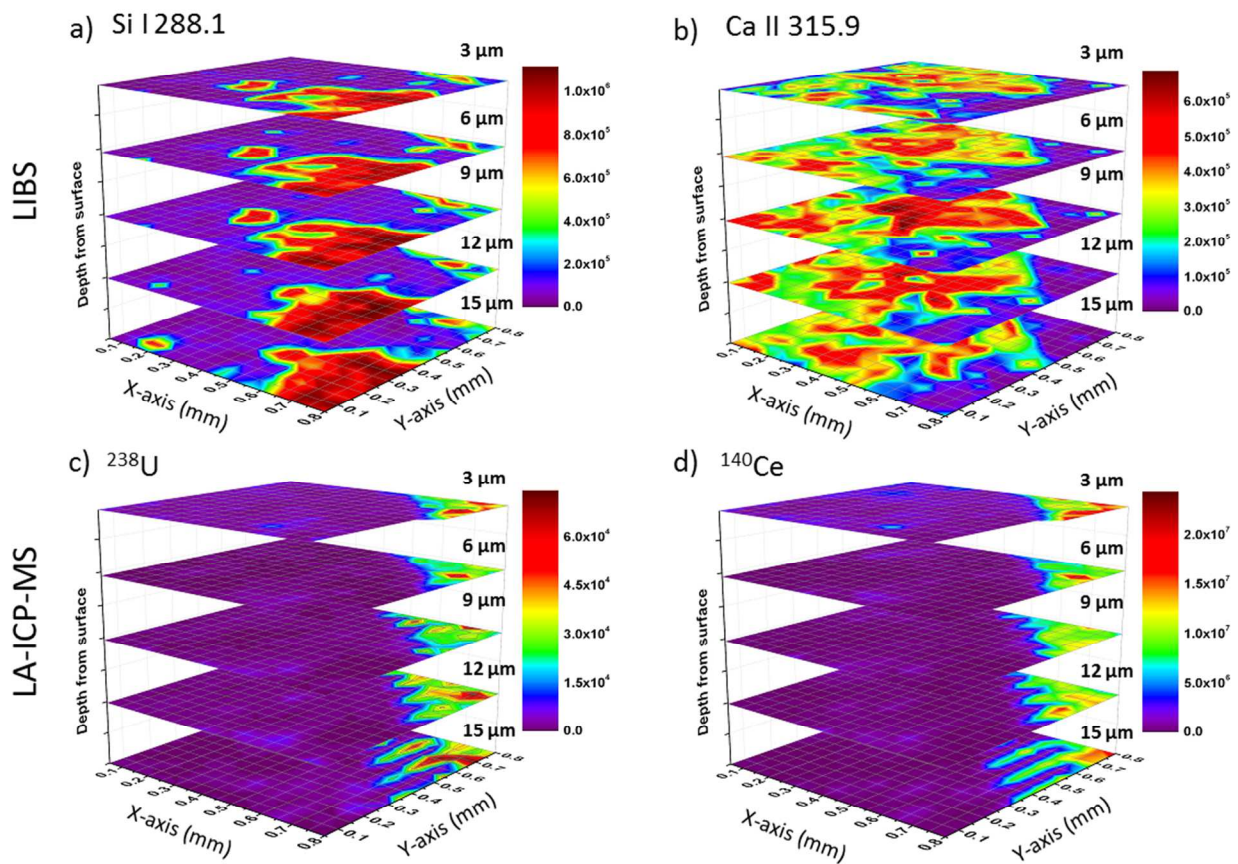


**Figure 4** Layer-by-layer contour elemental maps obtained by simultaneous LIBS/LA-ICP-MS.

(a)-(b) LIBS and (c)-(d) LA-ICP-MS maps as a function of depth.

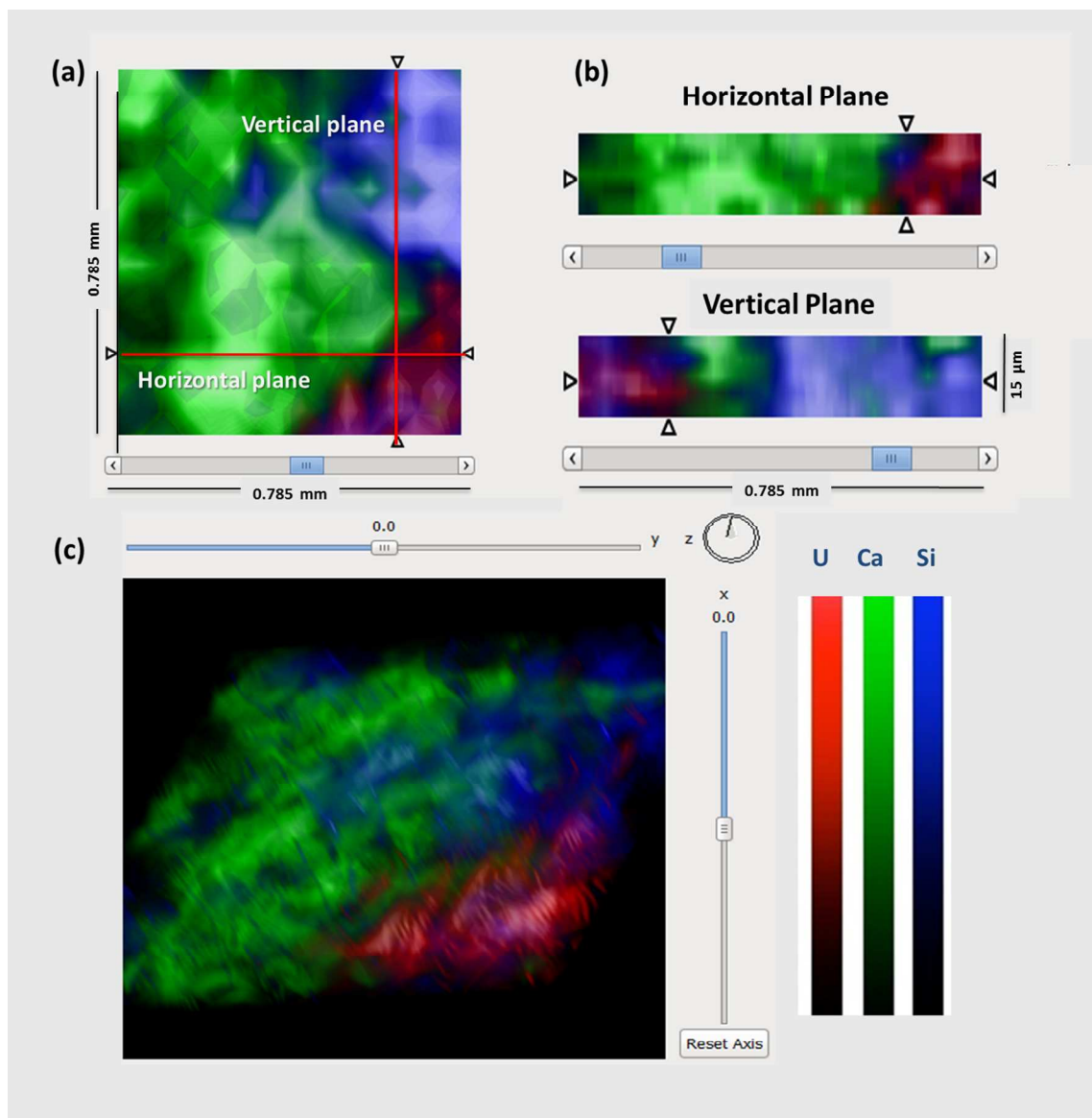


**Figure 5.** Merged overlay of U, Ca and Si maps. (a) 2D layer imaging, (b) 2D cross-sectional imaging and (c) 3D reconstruction of the elemental distribution in the *Bastnäs* rock matrix. All data are plotted using a linear color scale where the brightest colors represent the highest intensity. Lateral scale:  $0.785 \times 0.785 \text{ mm}^2$ , axial scale:  $15 \text{ }\mu\text{m}$ .

**References:**

- 1 B. Hattendorf, C. Latkoczy, and D. Gunther, *Anal. Chemistry* 2003, **75**(15), 341A-347A
- 2 R. E. Russo, X. L. Mao, H. Liu, J. Gonzalez, and S. S. Mao, *Talanta* 2002, **57**, 425–451.
- 3 E. Russo, X. L. Mao, C. Y. Liu, and J. Gonzalez, *J. Anal. At. Spectrom.* 2004, **19**, 1084–1089.
- 4 J. Koch and D. Gunther, *Appl. Spectrosc.* 2011, **65**, 155–162.
- 5 J.S. Becker, M. Zoriy, A. Matusch, B. Wu, D. Salber, C. Palm and J.S. Becker, *Mass Spectrom. Rev.* 2010, **29**, 156–175.
- 6 M. del Rosario Flórez, M. Aramendia and M. Resano, *J. Anal. At. Spectrom.* 2013, **28**, 1005-1015.
- 7 J. Elteren, A. Izmer, M. Šala, E.F. Orsega, V.S. Šelih, S. Panighello and F. Vanhaeckeb, *J. Anal. At. Spectrom.* 2013, **28**, 994-1004.
- 8 M Vašinová Galiová, M Nývltová Fišáková, J Kynický, L Prokeš, H Neff, A Z Mason, P Gadas, J Košler and V Kanický, *Talanta* 2013, **105**, 235–243.
- 9 J. Woodhead, J. Hergt, S. Meffre, R.R. Large, L. Danyushevsky and S. Gilbert, *Chem. Geol.* 2009, **262**, 344–354.
- 10 R. Thomas, *Practical Guide to ICP-MS: A Tutorial for Beginners, Third Edition (Practical Spectroscopy)*, CRC Press, Third. 2004.
- 11 Y. Orihashi and T. Hirata, *Geochem. J.* 2003, **37**, 401-412.
- 12 H.G. Dill, A. Gerdes and B. Weber, *Mineral. Mag.* 2007, **71**, 371–387.
- 13 Ian J Orland, Yuval Burstyn, Miryam Bar-Matthews, Reinhard Kozdon, Avner Ayalon, Alan Matthews and John W Valley, *Chem. Geol.* 2014, **363**, 322–333.

- 1  
2  
3  
4  
5 14 M.-L. C. Sirbescu, E.G. Krukowski, C.Schmidt, R. Thomas, I.M. Samson and R.J. Bodnar,  
6  
7 *Chem. Geol.* 2013, **342**, 138–150.  
8  
9 15 D. W. Hahn and N. Omenetto, *Appl. Spectrosc.* 2012, **66**, 347–419.  
10  
11 16 D. W. Hahn and N. Omenetto, *Appl. Spectrosc.* 2010, **64**, 335A–366A.  
12  
13 17 R. E. Russo, T. W. Suen, A. A. Bol'shakov, J. H. Yoo, O. Sorkhabi, X. L. Mao, J. Gonzalez,  
14  
15 D. Oropeza, and V. Zorba, *J. Anal. At. Spectrom.* 2011, **26**, 1596-1603.  
16  
17 18 M. Galiová, J. Kaiser, K. Novotný, J. Novotný, T. Vaculovič, M. Liška, R. Malina, K.  
18  
19 Stejskal, V. Adam and R. Kizek, *Appl Phys A* 2008, **93**, 917–922.  
20  
21 19 J. Kaiser, M. Galiová, K. Novotný, R. Červenka, L. Reale, J. Novotný, M. Liška, O.  
22  
23 Samek, V. Kanický, A. Hrdlička, K. Stejskal, V. Adam and R. Kizek, *Spectrochim. Acta B*  
24  
25 2009, **64**, 67–73.  
26  
27 20 K. Novotný, J. Kaiser, M. Galiová, V. Konečná, J. Novotný, R. Malina, M. Liška, V.  
28  
29 Kanický and V. Otruba, *Spectrochim. Acta B* 2008, **63**, 1139–1144.  
30  
31 21 M. Galiova, J. Kaiser, K. Novotny, M. Hartl, R. Kizek and P. Babula, *Microsc. Res. Techniq.*  
32  
33 2011, **74**, 845–852.  
34  
35 22 C. Latkoczy, T. Ghislain, *J. Anal. At. Spectrom.* 2006, **21**, 1152–1160.  
36  
37 23 C.L. Lin, Ching-Hao Hsieh, J.D. Miller, *Miner. Metall. Proc.* 2013 **30** 10-17.  
38  
39 24 V. Zorba, X. Mao and R. E. Russo, *Spectrochim. Acta B* 2011, **66**, 189-192.  
40  
41 25 R.E. Russo, A.A. Bol'shakov, X. Mao, C.P. McKay, D.L. Perry and O. Sorkhabi,  
42  
43 *Spectrochim. Acta B* 2011, **66**, 99–104.  
44  
45  
46  
47  
48  
49  
50  
51  
52  
53  
54  
55  
56  
57  
58  
59  
60